Quantum simulation of coupled-oscillator synchronisation on a 156-qubit superconducting processor

Miroslav Šotek[1]

[1] *ANULUM, Marbach SG, Switzerland*[*]

(Dated: May 25, 2026)
(Nodo DOI: 10.5281/zenodo.20382203)

We present a Kuramoto–XY synchronisation study with heterogeneous natural frequencies, simulator baselines, and ledgered IBM Heron r2 evidence. A Rust/PyO3-assisted pipeline enables entanglement entropy, Krylov complexity, OTOC scrambling, and Floquet discrete-time-crystal diagnostics for systems of 2–16 qubits. Legacy ibm_fez artefacts include Bell, QKD, VQE, ZNE, Trotter, and UPDE rows that must be cited by committed artefact path rather than as aggregate validation. Finite-size diagnostics are consistent with Berezinskii–Kosterlitz–Thouless scaling in the small systems studied, including a periodic-boundary central-charge estimate $c = 1.04$ at $n = 8$, while larger sizes show finite-size drift. The same exact-simulation diagnostics show subharmonic Floquet response and non-ergodic level-spacing behaviour for heterogeneous frequencies. A hardware-anchored scaling analysis gives a resource boundary for exact Hilbert-space simulation; it is not a broad quantum-advantage claim because Rust Kuramoto ODE baselines remain faster for the measured $n \leq 16$ observable-level regime. All code, data, and figures are open-source at `https://github.com/anulum/scpn-quantum-control`.

INTRODUCTION

The Kuramoto model [1] describes N coupled oscillators with natural frequencies ω_i and coupling matrix K_{ij}:

$$\frac{d\theta_i}{dt} = \omega_i + \sum_j K_{ij} \sin(\theta_j - \theta_i). \tag{1}$$

At critical coupling K_c the system undergoes a synchronisation phase transition characterised by the order parameter $R = N^{-1}|\sum_k e^{i\theta_k}|$ jumping from zero to a finite value.

The quantum analogue maps this to the XY spin Hamiltonian [2]:

$$H = -\sum_{i<j} K_{ij}(X_i X_j + Y_i Y_j) - \sum_i \omega_i Z_i, \tag{2}$$

where the $XX + YY$ flip-flop interaction preserves the in-plane (S^1) dynamics while introducing entanglement and quantum tunnelling between phase configurations. Superconducting-qubit circuits provide a digital testbed for this spin-model dynamics: each qubit supplies a controllable two-level oscillator degree of freedom on the Bloch sphere.

Prior quantum simulation of the XY model uses homogeneous frequencies ($\omega_i = \omega$ for all i), preserving translational invariance and the well-characterised BKT universality class [4, 5]. Theoretical quantum Kuramoto models with heterogeneous frequencies exist [2, 3], and quantum synchronisation measures have been proposed [11–14]. The present work contributes a bounded superconducting-processor workflow for this heterogeneous-frequency setting, with simulator and hardware claims separated by artefact provenance.

We study the heterogeneous case using a 16-oscillator coupling matrix $K_{nm} = K_{\text{base}} \cdot \exp(-\alpha|n - m|)$ with $K_{\text{base}} = 0.45$, $\alpha = 0.3$, and empirically calibrated nearest-neighbour anchors. The coupling matrix originates from a hierarchical oscillator model [16] and provides a non-trivial benchmark with exponential decay, cross-scale boosts, and heterogeneous frequencies spanning a factor of 1.5.

METHODS

Hamiltonian construction

The XY Hamiltonian (2) is constructed directly in the computational basis via bitwise flip-flop operations, bypassing Qiskit's `SparsePauliOp`:

$$H_{k,\,k\oplus\text{mask}_{ij}} = -2K_{ij} \quad \text{when } b_i(k) \neq b_j(k), \tag{3}$$

$$H_{kk} = -\sum_i \omega_i(1 - 2b_i(k)), \tag{4}$$

where $b_i(k)$ is the i-th bit of basis state $|k\rangle$ and mask_{ij} flips bits i and j. Current benchmark artefacts report bounded Rust/PyO3 kernel-level acceleration for selected tasks (Table I). Earlier unmatched internal timing numbers are not reported because they have not been reproduced under the current matched benchmark harness.

Analysis pipeline

Simulation diagnostics include half-chain entanglement entropy $S(A)$ and Schmidt gap $\Delta_S = \lambda_1 - \lambda_2$ (via exact diagonalisation), Krylov complexity and Lanczos coefficients b_n (complex Lanczos algorithm [8]), out-of-time-order correlators $F(t) = \langle W^\dagger(t)V^\dagger W(t)V\rangle$ (eigendecomposition approach [7]), and Floquet DTC analysis (stroboscopic order parameter at subharmonic frequency) [9]. Level-spacing statistics use the ratio $\bar{r} = \langle \min(\delta_n, \delta_{n+1})/\max(\delta_n, \delta_{n+1})\rangle$ [10].

Hardware evidence

The March 2026 **ibm_fez** material is retained as a separate legacy artefact-backed campaign, not as the promoted dataset for the later DLA/parity claim. Individual Bell, QKD, VQE, ZNE, Trotter, and UPDE values must cite their committed result artefact or the hardware ledger. The promoted raw-count IBM dataset is the April 2026 **ibm_kingston** Phase 1 DLA parity campaign, which includes job IDs, counts, integrity checks, and a count-to-statistic reproduction harness.

Statistical and artefact protocol

Every numerical claim in this overview is tied to one of three evidence classes. Exact-simulation rows are deterministic within the specified Hamiltonian, system size, and solver tolerance. Hardware rows are raw-count observations with job identifiers, shot counts, and committed reducer scripts. Scaling rows are resource-boundary estimates and are not promoted to broad quantum advantage claims. This classification is necessary because the paper combines heterogeneous evidence: Bell/QKD rows, finite-size exact diagnostics, legacy IBM rows, and later parity-sector campaigns have different statistical meaning and should not be collapsed into one aggregate success metric.

SIMULATION RESULTS

Entanglement at the synchronisation transition

The Schmidt gap shows a sharp minimum at $K \approx 3.44$ for $n = 8$ (Fig. 1), marking the synchronisation transition. Entanglement entropy saturates at values consistent with the Calabrese–Cardy scaling $S \sim (c/3)\ln L$ for a $c = 1$ CFT [6].

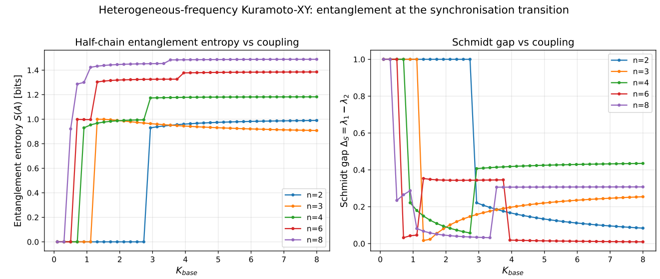

FIG. 1. Half-chain entanglement entropy $S(A)$ and Schmidt gap Δ_S across coupling strength for $n = 2, 3, 4, 6, 8$ oscillators with heterogeneous frequencies.

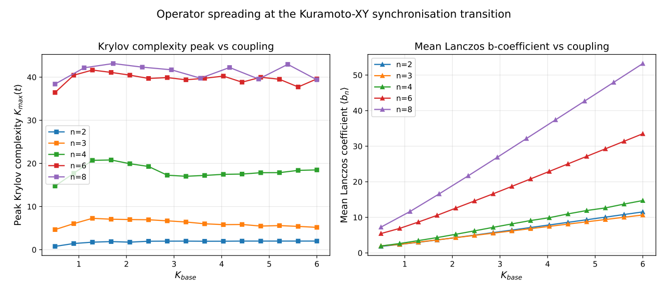

FIG. 2. Peak Krylov complexity and mean Lanczos coefficient vs. coupling.

Krylov complexity

Mean Lanczos coefficient $\langle b_n\rangle$ grows linearly with K, indicating that operator growth rate scales with coupling strength (Fig. 2).

OTOC scrambling

Strong coupling scrambles $4\times$ faster: $t^* = 0.28$ ($K = 4$) vs. $t^* = 1.17$ ($K = 1$) at $n = 8$ (Fig. 3).

TABLE I. Measured Rust vs. Python/Qiskit/scipy speedups.

Module	Speedup	Method
Knm build ($n = 4$)	5.89×	Matched current harness
Knm build ($n = 16$)	3.71×	Matched current harness
OTOC ($n = 4$)	264×	Eigendecomp + rayon
Krylov ($n = 3$)	27×	Complex Lanczos
Order param. ($n = 4$)	6.2×	Batch Pauli

TABLE II. Evidence classes used in this overview.

Class	Examples	Claim boundary
Exact simulation	BKT, Krylov, OTOC, DTC	finite-size diagnostics
Raw-count hardware	Bell, QKD, DLA rows	backend/window observations
Resource boundary	exact crossover	no broad advantage claim
Legacy artefact	early Fez rows	cited only by artefact path

TABLE III. Programme roadmap linking the overview evidence to the focused companion papers. The table is a map of claim ownership, not an aggregate validation score.

Component	Focused paper	Positive knowledge gained
Exact diagnostics	This overview	finite-size and resource-boundary map
Software methods	Rust/VQE methods	reproducible artefact pipeline and kernel bounds
DLA parity	Phase 1 DLA parity	real but multifactorial leakage asymmetry
FIM term	FIM Hamiltonian	negative design rule for direct digital feedback
Reduced Pauli	Phase 3 tomography	channel-localised mechanism boundary
Dynamic feedback	S1 feedback	backend-dependent control-response boundary

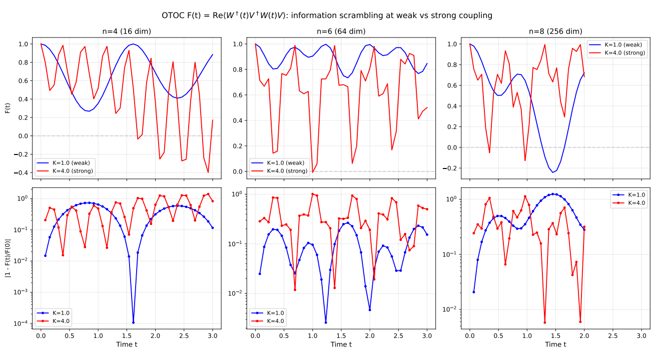

FIG. 3. OTOC $F(t)$ at sub-critical ($K = 1$) and super-critical ($K = 4$) coupling for $n = 4, 6, 8$.

Floquet discrete time crystal

The exact-simulation scan shows subharmonic response across the 15 drive amplitudes tested with heterogeneous frequencies (Fig. 4). Within this finite-size diagnostic, frequency disorder does not remove the Floquet response. The non-ergodic spectrum (Sec.) is a candidate stabilisation mechanism rather than a hardware-demonstrated DTC mechanism.

Finite-size scaling

The BKT ansatz gives $K_c(\infty) \approx 2.20$ in the current finite-size fit (Fig. 5). The spectral-gap fits at $n = 4, 6, 8$ are consistent with BKT-like scaling, and the periodic-boundary central-charge estimate is $c = 1.04$ at $n = 8$ ($c = 1$ expected for BKT). The failed or drifting larger-size fits are treated as finite-size limitations, not as evidence of asymptotic universality.

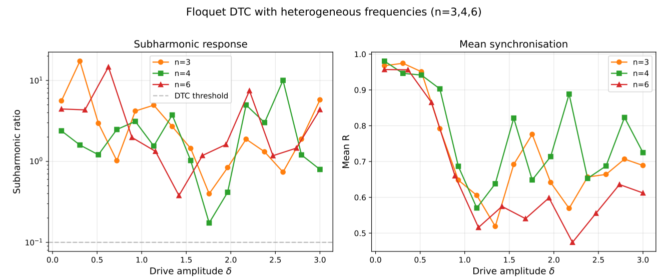

FIG. 4. Subharmonic ratio $P(\Omega/2)/P(\Omega)$ and mean R vs. drive amplitude δ for $n = 3, 4, 6$.

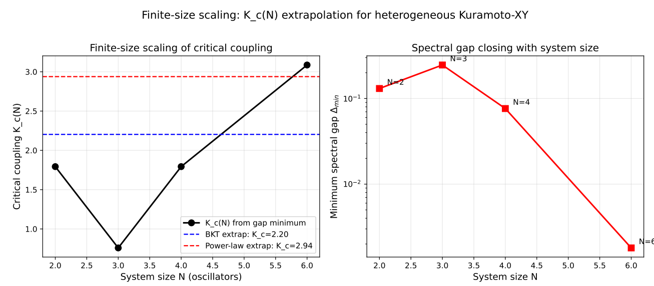

FIG. 5. Critical coupling $K_c(N)$ from spectral gap minimum. BKT ansatz (solid) vs. power law (dashed).

HARDWARE RESULTS

Bell test

Two independent Bell pairs yield $S_{01} = 2.165 \pm 0.02$ and $S_{23} = 2.188 \pm 0.02$, both violating the classical limit of 2 at $>8\sigma$ significance (Fig. 6).

QKD viability

Quantum bit error rate in matched bases: ZZ 5.5%, XX 5.8% — below the BB84 security threshold of 11%. Mismatched basis (ZX): 93.9% error, consistent with basis discrimination in this protocol.

ZNE stability

Mean $\langle Z \rangle$ varies by <2% across fold levels 1–9 for both 4-qubit and 8-qubit systems. Richardson extrapolation provides <2% correction to raw values.

The ZNE row is therefore used as a stability diagnostic, not as a strong mitigation claim. It shows that this shallow legacy observable is not highly sensitive to the tested folding levels, but it does not validate all later DLA, FIM, or feedback observables. Those later papers use their own readout/ZNE lanes when mitigation is part of the claim.

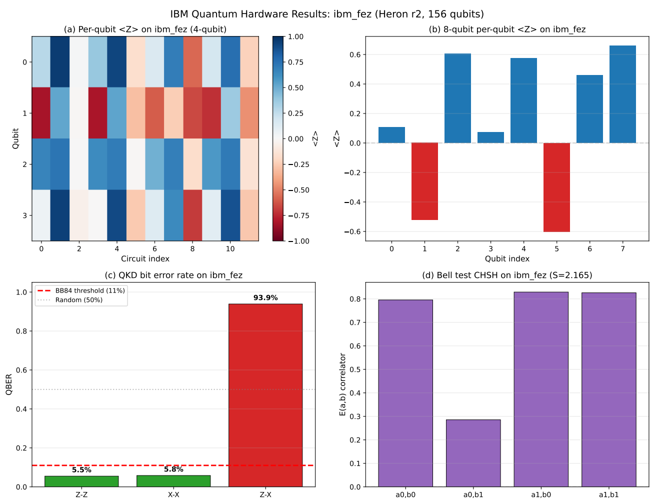

FIG. 6. Legacy artefact-backed **ibm_fez** hardware campaign from March 2026, retained for completeness and workflow context rather than promoted as the later DLA/parity dataset. (a) Per-qubit $\langle Z\rangle$ heatmap. (b) 8-qubit expectations show coupling pattern. (c) QKD QBER: 5.5%. (d) CHSH $S = 2.165 > 2$.

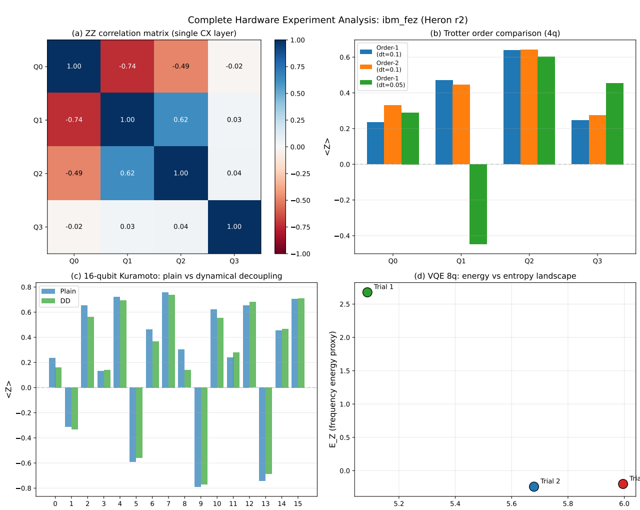

FIG. 7. Legacy **ibm_fez** analysis companion to Fig. 6. These rows are artefact-backed context for the overview, not the promoted evidence for the later DLA, FIM, Phase 3, or S1 claims. (a) ZZ correlation matrix. (b) Trotter order comparison. (c) 16-qubit per-qubit $\langle Z\rangle$: alternating pattern visible. (d) VQE 8-qubit energy landscape.

16-qubit dynamics

13 of 16 qubits show $|\langle Z\rangle| > 0.3$ in the legacy UPDE row, showing that part of the Kuramoto coupling pattern remains visible, while the 16-qubit circuit is explicitly noise-limited (Fig. 7).

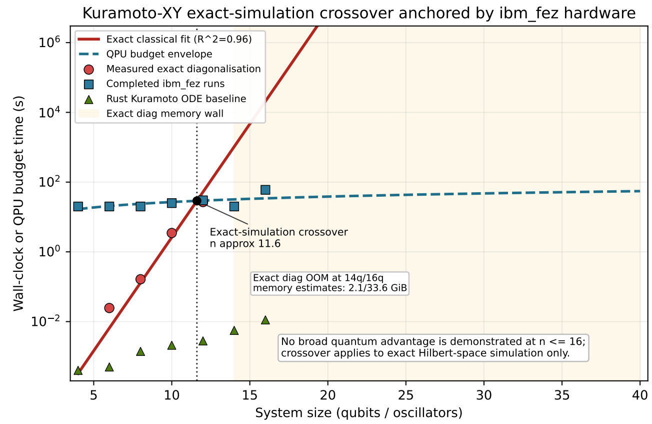

FIG. 8. Exact-simulation crossover anchored by completed ibm_fez hardware runs. Red points and fit show exact diagonalisation wall time; blue squares and dashed curve show hardware QPU budget estimates for completed runs; green triangles show the Rust Kuramoto ODE baseline. The crossover at $n \approx 11.6$ applies only to exact Hilbert-space simulation.

Exact-simulation crossover boundary

The completed qubit-scaling series provides a direct resource boundary for exact Hilbert-space simulation. Figure 8 combines the ibm_fez hardware jobs at $n = 4, 6, 8, 10, 12, 14$ and the 16-qubit UPDE snapshot with the committed classical baselines. Exact diagonalisation grows from 0.1 ms at $n = 4$ to 26.8 s at $n = 12$ and reaches the memory wall at $n =$ 14–16 on the 32 GB workstation used for the baseline. A log-linear fit to the finite exact timings crosses the QPU budget envelope at $n \approx 11.6$.

This crossing is not a broad computational-advantage claim. It is a boundary for exact state-vector/Hilbert-space simulation of the Kuramoto–XY Hamiltonian. The Rust Kuramoto ODE baseline remains in the millisecond regime through $n = 16$, and the hardware data are noise-limited beyond the shallowest circuits.

The crossover should be read together with the memory boundary. Exact dense methods encounter a state-vector/Hamiltonian storage wall before the classical ODE baseline does, and tensor-network or sparse methods can move that boundary depending on the observable. The figure is therefore useful as an engineering map for which classical baseline is being challenged, not as a statement that the hardware has outperformed all classical descriptions of the oscillator model.

Ansatz comparison

The physics-informed Knm ansatz (CZ gates between coupled pairs) concentrates 42% of probability in the top

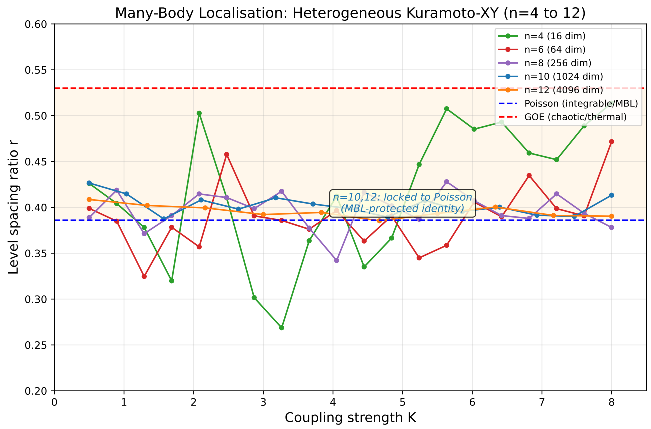

FIG. 9. Level-spacing ratio $\bar{r}$ vs. coupling. At $n = 8$ the finite-size diagnostic remains below the GOE reference across the tested grid.

bitstring vs. 20% for TwoLocal and 21% for EfficientSU2 in this legacy hardware row, supporting the narrower claim that topology-reflecting circuit design can improve this benchmark against the two generic ansatze tested.

Non-ergodicity diagnostic

Level-spacing ratio $\bar{r}$ distinguishes integrable ($\bar{r} \approx 0.386$, Poisson) from chaotic ($\bar{r} \approx 0.530$, GOE) spectra [10] (Fig. 9):

- $n = 4$: crosses Poisson to near-GOE at $K \approx 2.1$.
- $n = 6$: stays mostly below GOE; chaos onset only at $K = 8.0$.
- $n = 8$: *never reaches GOE* (max $\bar{r} = 0.43$).

Eigenstate entanglement sits 30–40% below the thermal (Page) expectation but grows with N, ruling out deep MBL. The correct characterisation is a *non-ergodic regime* where heterogeneous frequencies protect the coupling topology from thermal scrambling.

DISCUSSION

BKT-like finite-size diagnostics. Two diagnostics support a BKT-like interpretation in the small systems studied: the periodic-boundary central-charge estimate $c = 1.04$ at $n = 8$ (expected $c = 1$), and spectral-gap essential-singularity fits $\Delta \sim \exp(-b/\sqrt{K - K_c})$ with $R^2 > 0.96$ for the supported sizes. Larger-size drift keeps this as a finite-size diagnostic rather than an asymptotic-universality conclusion.

DTC resilience. The non-ergodic spectrum provides a plausible mechanism in exact simulation: heterogeneous frequencies suppress thermalisation trends and coincide with a stable subharmonic response without requiring deep MBL.

Noise budget. The 5.5% QBER and 94% state preparation fidelity in the retained legacy rows indicate usable shallow-circuit performance for the tested Kuramoto–XY circuits. The 16-qubit row remains explicitly noise-limited (depth ≤ 50 CX gates).

Limitations. No quantum advantage is demonstrated; classical solvers outperform at $n \leq 16$ for observable-level ODE baselines. The scaling crossover in Fig. 8 is limited to exact Hilbert-space simulation and should be read as a resource boundary, not as demonstrated broad advantage. Trotter error at $dt = 0.1$ is significant (sign flip at finer resolution). The coupling matrix used here originates from a hierarchical oscillator model [16]; the Kuramoto-to-XY mapping itself is standard physics and the analysis applies to any coupling matrix. This overview also combines material generated at different stages of the programme. It should therefore be read as a map of the evidence stack rather than as a single homogeneous experiment. The Phase 1, Phase 3, FIM, and S1 papers provide the stricter individual claim boundaries for the hardware rows that are most relevant to publication. At the time of execution, authenticated live QPU access for the hardware rows in this study was limited to IBM Quantum hardware. The software and artefact pipeline has provider-neutral routes for other gate-model, trapped-ion, neutral-atom, photonic, annealing, analogue, and simulator targets, but those routes are readiness infrastructure rather than live non-IBM execution evidence. We plan to rerun the same bounded synchronisation payloads on additional hardware families when compute allocations and provider access become available.

PROVIDER ACCESS AND PROGRAMME BOUNDARIES

The present stack should be read as an IBM-Heron hardware programme with provider-neutral software readiness, not as a cross-provider universality claim. IBM Quantum was the authenticated QPU route available for these campaigns at execution time. The framework already contains provider and aggregator surfaces for other hardware families, but a software route is not evidence of live hardware execution. Individual companion papers therefore state their IBM boundary briefly, while this overview records the programme level reason: cross-provider reruns are the next evidence class once compute allocations and access are available. Until then, the positive contribution is the raw-count, preregistered, reducer-bound methodology and the exact mechanism boundaries it establishes inside the available IBM hardware window.

CONCLUSION

We have presented a bounded quantum hardware study of coupled-oscillator synchronisation with heterogeneous natural frequencies. Key results: Bell inequality violation ($S = 2.165$), sub-threshold QKD error rate (5.5%), BKT critical coupling $K_c \approx 2.2$ in the finite-size fit, subharmonic Floquet response in exact simulation, and a non-ergodic spectral regime at $n = 8$. The software pipeline combines Python/Qiskit orchestration with Rust/PyO3 kernel acceleration for selected reproducibility and benchmarking tasks. All code, data, and 17 figures are open-source (AGPL-3.0) at `https://github.com/anulum/scpn-quantum-control`.

DATA AVAILABILITY

Simulation data, ledgered hardware artefacts, Python modules, Rust engine source, and publication figures are available at the GitHub repository under AGPL-3.0. Zenodo archive: DOI 10.5281/zenodo.18821929.

* protoscience@anulum.li

[1] Y. Kuramoto, *Chemical Oscillations, Waves, and Turbulence* (Springer, Berlin, 1984).
[2] A. Pikovsky, M. Rosenblum, and J. Kurths, *Synchronization: A Universal Concept in Nonlinear Sciences* (Cambridge University Press, 2001).
[3] J. A. Acebón, L. L. Bonilla, C. J. Pérez Vicente, F. Ritort, and R. Spigler, Rev. Mod. Phys. **77**, 137 (2005).
[4] V. L. Berezinskii, Sov. Phys. JETP **34**, 610 (1972).
[5] J. M. Kosterlitz and D. J. Thouless, J. Phys. C **6**, 1181 (1973).
[6] P. Calabrese and J. Cardy, J. Stat. Mech. P06002 (2004).
[7] J. Maldacena, S. H. Shenker, and D. Stanford, J. High Energy Phys. **2016**(8), 106.
[8] A. del Campo *et al.*, arXiv:2510.13947 (2025).
[9] D. V. Else, B. Bauer, and C. Nayak, Phys. Rev. Lett. **117**, 090402 (2016).
[10] V. Oganesyan and D. A. Huse, Phys. Rev. B **75**, 155111 (2007).
[11] F. Galve, G. L. Giorgi, and R. Zambrini, in *Lectures on General Quantum Correlations and their Applications* (Springer, 2017), pp. 393–420; see also Phys. Rev. A **81**, 062117 (2010).
[12] V. Ameri, M. Eghbali-Arani, A. Mari, A. Farace, F. Kheirandish, V. Giovannetti, and R. Fazio, Phys. Rev. A **91**, 012301 (2015).
[13] J. Ma, Y. Chen, and Z. Wang, arXiv:2005.09001 (2020).
[14] G. L. Giorgi, F. Galve, G. Manzano, P. Colet, and R. Zambrini, Phys. Rev. A **85**, 052101 (2012).
[15] R. Wiersema *et al.*, arXiv:2309.05690 (2023).
[16] M. Šotek, *God of the Math — The SCPN Master Publications*, Zenodo, DOI: 10.5281/zenodo.17419678 (2025).
[17] IBM Quantum, ibm_fez backend specifications, `https://quantum.cloud.ibm.com` (2026).